Structural, Magnetic, DFT, and Biological Studies of Mononuclear and Dinuclear Cu^{II} Complexes with Bidentate N-Heteroaromatic Schiff Base Ligands

Tamara Todorović,[a] Sonja Grubišić,[b] Matej Pregelj,[c] Marko Jagodič,[d] Sonja Misirlić-Denčić,[e] Marija Dulović,[e] Ivanka Marković,[e] Olivera Klisurić,[f] Aleksandar Malešević,[a] Dragana Mitić,[a] Katarina Anđelković,[a] and Nenad Filipović*[g]

[a] Department of General and Inorganic Chemistry, University of Belgrade – Faculty of Chemistry, Studentski trg 12–16, 11000 Belgrade, Serbia
[b] Center for Chemistry, IHTM, University of Belgrade, Njegoševa 12, 11001 Belgrade, Serbia
[c] Jožef Stefan Institute, Jamova 39, 1000 Ljubljana, Slovenia
[d] Institute of Mathematics, Physics and Mechanics, Jadranska 19, 1000 Ljubljana, Slovenia
[e] Institute of Medical and Clinical Biochemistry, Faculty of Medicine, University of Belgrade, Pasterova 2, 11000 Belgrade, Serbia
[f] Department of Physics, Faculty of Sciences, University of Novi Sad, Trg Dositeja Obradovic´a 4, 21000 Novi Sad, Serbia
[g] Department of Chemistry and Biochemistry, Faculty of Agriculture, University of Belgrade, Nemanjina 6, 11000 Belgrade, Serbia E-mail: nenadf.chem@gmail.com http://www.agrif.bg.ac.rs/profiles/view/242

Keywords: Copper / Magnetic properties / Density functional calculations / Medicinal chemistry / Cytotoxicity / Apoptosis

Copper(II) complexes with the condensation derivative of methyl hydrazinoacetate and 2-acetylpyridine were synthesized. The X-ray crystal structures for both complexes revealed that they are polymerized isomers. A common feature of both complexes is the bidentate coordination of the ligand by one hydrazone and one pyridine nitrogen atom. In the monomeric complex, the copper(II) center is tetracoordinate, whereas dimerization through chlorido bridges results in a pentacoordinate arrangement about the metal ions in the dimer. The electronic and magnetic properties of both complexes are discussed on the basis of their X-ray structures, electron paramagnetic resonance (EPR) spectroscopy studies, and superconducting quantum interference device (SQUID) magnetization measurements combined with DFT calculations. Magnetostructural comparisons with structurally similar copper(II) complexes are also provided, and a possible correlation has been established. The antitumor activities of the CuII complexes

were investigated against six different cancer cell lines, and the results suggest that the antiglioma action of the dimeric species is based on oxidative-stress-mediated phosphatidylserine externalization and caspase activation, which indicate apoptosis.

Introduction

Copper complexes with multidentate hydrazone ligands possess a broad spectrum of biological activity and are less toxic than platinum-based anticancer drugs.[1] It has been suggested that copper species could overcome resistance to cisplatin owing to the different mechanisms of action of copper species in comparison to those of cisplatin and other platinum-based drugs, which bind covalently to DNA. Although DNA is still the main target for many biologically active copper complexes, other biomacromolecules such as topoisomerase I and II and proteasome multiprotein complex have been identified as possible cellular targets.[1] Noncovalent interactions of copper complexes with the DNA double helix occur through intercalation, electrostatic interactions, and major/minor groove binding, and DNA cleavage promoted by copper species occurs through a Fentontype reaction or hydrolytic cleavage mechanism.[1] As a consequence of induced DNA damage, cellular processing can trigger apoptotic cell death; however, very few papers report the molecular basis for the mode of action of copper complexes, such as the involvement of caspase activation in copper-complex-mediated cell death.[1–4] The type of ligand and the coordination geometry play important roles in determining the cytotoxic action of copper complexes.[1]

Multidentate hydrazone ligands possess a wide spectrum of biological activities, which are increased significantly by complexation to metal ions.[5,6] Moreover, some hydrazone

complexes have catalytic properties and can be used as model systems for enzymes; some di- and oligonuclear hydrazone complexes can serve as molecular-based information-storage devices.[7–10] The focus of our previous research has been the coordination properties of N-heteroaromatic hydrazones (qahaOEt, aphaOEt, and fphaOEt) derived from ethyl hydrazinoacetate (haOEt) and the N-heteroaromatic carbonyl compounds 2-quinolinecarbaldehyde (2qa), 2-acetylpyridine (2ap), and 2-formylpyridine (2fp).[11–15] The data obtained by a single-crystal X-ray diffraction (XRD) and nuclear magnetic resonance spectroscopy showed that the ligands qahaOEt, aphaOEt, and fphaOEt (Scheme 1) were coordinated to the metal centers exclusively N,N bidentately in the solid state and in solution through the formation of five-membered chelate rings. The obtained complexes were mononuclear, except for a dinuclear CuII complex with the qahaOEt ligand. To the best of our knowledge, only a few dinuclear hydrazone complexes, resulting from the dimerization of mononuclear units, have been studied from the aspect of the thermodynamics of the dimerization process through the determination of the XRD structures of both the monomeric and dimeric forms.[16] In most cases, the obtained complexes were unexpected products and formed through uncontrolled self-assembly.

Herein, we report the synthesis, XRD structures, and variable-temperature magnetic behavior of monomeric and dimeric copper(II) complexes **1** and **2** with the in situ obtained aphaOMe ligand (Scheme 1). The obtained complexes are polymerized isomers. The conditions that allow the formation of the monomeric and dimeric compound have been explored. The magnetic properties of the obtained complexes **1** and **2** as well as those of the structurally similar complexes [CuCl2(fphaOEt)] (**3**), [CuCl2(aphaOEt)] (**4**), and [Cu2Cl4(qahaOEt)2] (**5**; Scheme 1)[14] are explored and discussed on the basis of electron paramagnetic resonance (EPR)

spectroscopy and superconducting quantum interference device (SQUID) magnetometry studies combined with DFT calculations. An investigation of the cytotoxic action of the copper complexes was performed with six tumor cell lines. Furthermore, in deciphering the mode of cytotoxic action of the most potent complexes, we investigated the production of reactive oxygen species (ROS), as well as caspase activation, phosphatidylserine externalization, and cell-cycle disturbances as the hallmarks of apoptotic cell death.

Results and Discussion

Synthesis of 1 and 2 and their Interconversion

Complexes **1** and **2** were obtained from the reaction of a methanolic solution of 2ap, haOEt·HCl, and $CuCl_2 \cdot 2H_2O$. During the reaction, the transesterification of ethyl to methyl ester resulted in the formation of complexes with the ligand aphaOMe. Triclinic green crystals of complex **1** separated over 3 d at ambient temperature and were removed, and the mother liquor was then allowed to slowly evaporate at the same temperature. More green crystals separated; however, these were mixed with much smaller brown crystals of **2**. The mother liquor was decanted, and the brown crystals were segregated by hand from the larger green crystals under a stereomicroscope. Further evaporation of the mother liquor produced only brown crystals. To study the effect of temperature on the molecular structure, the initial reaction mixture was cooled to room temperature after reflux and divided in two equal parts, which were kept in a freezer and a refrigerator (ca. –20 and 10 °C, respectively). Only needle-shaped brown crystals were obtained from the solution kept in the freezer, whereas a mixture of larger green (ca. 80 wt.-%)

and smaller brown crystals (ca. 20 wt.-%) was obtained from the solution kept in the refrigerator. Additionally, when a hot reaction mixture was placed in the refrigerator for a few hours, only brown crystals were obtained. Interestingly, **1** and **2** are not readily interconvertible: a methanolic solution of **1** yielded a mixture of **1** and **2** after slow evaporation at room temperature, but the same solution at low temperature (ca. –20 °C) produced only **2**. On the other hand, a methanolic solution of **2** produced exclusively **2** regardless of the crystallization temperature. These results indicate that the crystallization temperature plays a partial role in the final structure of the product.

To check whether one isomer could be converted into the other in the solid state and to detect possible phase transitions with increasing temperature, powder samples of **1** and **2** were investigated by X-ray diffraction in a reflexive Bragg–Brentano θ–2θ geometry. The obtained diffraction profiles for **1** and **2** at different temperatures are shown in Figures S1 and S2 (Supporting Information). Both samples have unchanged angular positions for the three most intense and distinct reflection peaks, which are located at 2θ = 8.46, 10.86, and 25.20° for **1** and 2θ = 10.40, 21.15, and 27.25° for **2**. These results strongly indicate the existence of an unchanged and unique phase during the temperature increment. Therefore, no dimerization of the monomeric complex **1** to the dimeric complex **2** or vice versa occurred at temperatures up to 110 °C.

Analysis of the Crystal Structures

The pertinent crystallographic data for the structures of **1** and **2** are given in Table S1. ORTEP drawings of the molecular structure of the complexes are depicted in Figure 1, and selected bond lengths and angles are given in Table 1. The common feature of both complexes is

the bidentate coordination of the aphaOMe ligand through one hydrazone and one pyridine nitrogen atom. In the monomeric complex **1**, the copper(II) ion is tetracoordinate. In contrast, dimerization through chlorido bridges results in a pentacoordinate arrangement about the copper(II) ions in **2**. However, all of the respective bonds not directly involved in dimerization are similar in both complexes (Table 1).

The structure of **1** consists of monomeric [$CuCl_2$- (aphaOMe)] units (Figure 1, a). The tetrahedral arrangement around the copper(II) center is distorted and very much flattened. As the angle between the plains through the Cl(1)–Cu(1)–Cl(2) and N(1)–Cu(1)–N(2) atoms is 21.7(2)° and the Cu(1) center does not deviate significantly from the basal plane through N(1)–N(2)–Cl(1)–Cl(2) [0.0486(2) Å], the geometry around the metal center in the mononuclear complex **1** can be described as distorted square-planar. The τ4 geometry index[17] of 0.24 for **1** further supports the assignment of a distorted square-planar geometry. There are no significant interactions at the axial positions, and the closest contacts of Cu(1) are 3.013(3) and 3.0987(11) Å for N(3) (2 – *x*, 1 – *y*, 1 – *z*) and Cl(1) (1 – *x*, 1 – *y*, 1 – *z*), respectively. However, these weak interactions are responsible for the formation of 1D polymeric chains parallel to the *a* axis in the crystal structure of **1** (Figure S3).

In the dinuclear complex **2** (Figure 1, b), each copper(II) center is pentacoordinate. The complex has a heavily distorted square-pyramidal geometry, as indicated by the value of the angular structural parameter τ5 (0.44)[18] and the distance of the Cu(1) atom from the basal plane [Cl(1)–Cl(2)– N(2)] of 0.046(2) Å. The apical sites are occupied by Cl(2)*i* (*i* = 2 – *x*, 1 – *y*, 1 – *z*) and N(1). As previously observed for other dimeric Cu^{II} species with halogen bridges,[14,19,20] one strong and one weak Cu–Cl interaction are present in **2** [Cu(1)⋯Cl(2) 2.2812(9) Å and Cu(1)⋯Cl(2)*i* 2.6636(9) Å]. Likewise, the Cu–(μ-Cl)$_2$–Cu skeleton formed by

dimerization exhibits rhomboidal geometry. The relatively short Cu(1)···Cu(1)*i* distance of 3.638(1) Å is reflected in the magnetic properties of the compound (vide infra). The crystal packing of **2** is dominated by the π–π interactions of the pyridine fragments with a centroid–centroid (Cg–Cg*i*; *i* = 1 – *x*, 1 – *y*, 1 – *z*) distance between the stacked rings of 3.914(2) Å. The corresponding displacement angle of 24.7° is in accordance with a respective shift of 1.637 Å, which indicates an almost perfect face-to-face alignment.[21] In addition, bifurcated C–H···O interactions (listed in Table S2) further stabilize the supramolecular assembly in **2**. The stacking and C–H···O interactions expand the dinuclear units into 1D supramolecular chains running along the [100] direction (Figure S4).

Several examples of polymerized isomers in coordination chemistry have been reported.[22–24] A comparison of the inner coordination sphere of the copper atoms in **1** and **2**, that is, in the monomer and the dimer, respectively, through least-squares fits of the aromatic frames is depicted in Figure 2. The overlay reveals a decisive separation of the ligand side chains by ca. 64.5°, probably because of the involvement of O(1) in the bifurcated C–H···O interactions in the crystal packing of **2**.

On the other hand, an analogous comparison of monomeric complexes **1** and **4** [Cambridge Structural Database (CSD) refcode QOWWUV][14,16] shows that the two match almost exactly. Specifically, the separation among the side chains is only ca. 5° (Figure S5), and the crystal packings of these two complexes are also very similar (Figure S6). Apparently, the substitution of the Et group from the ligand side chain in **4** with the Me group in **1** affects neither the molecular nor the crystal structure. However, small structural differences between the bidentate ligands aphaOMe and fphaOEt (Scheme 1) cause significant differences in the molecular and crystal structures of **1** and **3** (CSD refcode QOWWOP).[14,16] This is evident

from the superposition of the aromatic frames of **1** and **3** (Figure S7), which shows that the separation of the ligand side chains amounts to ca. 54°. The crystal packing of both **1** and **3** is characterized by the formation of 1D chains; however, in contrast to those in **1**, the chains in the crystal structure of **3** are formed through weak coordinative bonds with the in-plane chlorido ligand from the neighboring complex unit.[14] For the dihalo-bridged dinuclear Cu^{II} complexes **2** and **5** (CSD refcode QOWXAC),[14,16] although all copper(II) centers are pentacoordinate, there is a difference in the geometry of the complexes: **2** has a heavily distorted square-pyramidal geometry, whereas the geometry in **5** is trigonal bipyramidal.[14] The geometries of the Cu–(μ-Cl)2–Cu skeleton, formed by dimerization in both complexes, are similar (Figure S8).

Electronic Absorption Spectroscopy and Molar Conductivity Measurements

The UV/Vis absorption spectra of the Cu^{II} complexes in dimethyl sulfoxide/H_2O (DMSO/H_2O, 0.5:100 v/v) solutions at 298 K are shown in Figure S9, and the significant electronic spectral bands are presented in Table S3. The common features of the spectra of all complexes are the strong bands observed below λ = 350 nm associated with the pyridine/quinoline rings (n$R\pi^*$ transitions) and Npyridine/NquinolineRCu and ClRCu charge-transfer bands.[25] For essentially tetragonal or square-planar Cu^{II} complexes, the ground state (in D_{4h} notation) is $^2B_{1g}$ and the three possible excited states are $^2A_{1g}$, $^2B_{2g}$, and ^2E_g. Therefore, three spin-allowed d–d transitions are possible to $b_{1g}(d_{x2-y2})$ from $a_{1g}(d_{z2})$, $b_{2g}(d_{xy})$, and $e_g(d_{xz},d_{yz})$, respectively. However, as the three lower occupied states are very close in energy, it is often difficult to resolve the bands into separate components and to confirm their order experimentally. For square-pyramidal (C_{4v}) complexes, the same three d–d transitions, namely, from $a_1(d_{z2})$, $b_2(d_{xy})$, and $e(d_{xz},d_{yz})$ to $b_1(d_{x2-y2})$, are possible and often cannot be resolved for the same reasons. In both stereochemistries, a departure from regular symmetry as well as the metal–

ligand π bonding influences the shape of the broad absorption band. In the trigonal-bipyramidal (D_{3h}) configuration, the ground state is $^2A'_1$ (d_{z2}), and the visible absorption band consists of two closely overlapped components stemming from the $^2E'$ and $^2E''$ excited states. The spectra of square-planar complexes **1**, **3**, and **4** exhibit weak d–d bands centered at $\lambda \approx 745$ nm. In the spectrum of **2**, a broad asymmetric maximum at $\lambda = 786$ nm, attributed to a d–d transition, can be observed. This transition is consistent with the distorted square-pyramidal geometry ($\tau_5 = 0.44$) but has a slightly lower energy than expected, owing to a high distortion with a tetrahedral twist of the square base (33°).[26] Complex **5** with $\tau_5 = 0.71$[14] displays a single broad d–d transition at 942 nm, consistent with a distorted trigonal-bipyramidal geometry. The aqueous solution behavior of **1**–**5** with respect to hydrolysis was also studied in DMSO/H_2O (0.5:100 v/v) at 298 K over 24 h by UV/Vis spectroscopy and by molar conductivity measurements in the same solvents at 298 K over 10 h. The complexes were quite stable, as can be seen from their electronic absorption spectra (Figure S10) and the plots of molar conductivity versus time (Figure S11). The solid-state diffuse reflectance spectra of **1** and **2** are depicted in Figure S12. The solid-state reflectance spectra match those determined for the complexes in the solution; therefore, structural changes of the complexes do not occur under the influence of the solvent(s). The XRD, UV/Vis spectroscopy, and molar conductivity results indicate that the structures of the complexes are the same in solution and in the solid state.

Magnetic Behavior

The relevant parameters obtained from the EPR spectra (Figure S13) of Cu^{II} complexes ($S = 1/2$) **1**–**5** are summarized in Table 2. The derived g values imply that the Cu^{II} centers in **2** and **5** are located in strongly distorted orthorhombic environments, whereas the Cu^{II} centers in **1**,

3, and **4** have tetragonal geometries, in agreement with the crystallographic data. The spectra for **1** and **4** show a weak hyperfine splitting; however, the hyperfine splitting cannot be resolved for **2**, **3**, and **5**, probably because of stronger spin– spin interactions. The latter also produces more pronounced line broadening in **2**, **3**, and **5**, in accord with the dimeric nature of the Cu^{II} species in **2** and **5**. However, the strong spin–spin interaction in **3** can be explained by the fact that the chains of monomers are bridged by a single chlorido ligand. Finally, we note that the derived room-temperature EPR susceptibilities comply with the values obtained from the magnetic susceptibility measurements (Table 2); therefore, the EPR signals are intrinsic. This also reflects in the effective magnetic moments per Cu^{II} ion obtained from the EPR measurements of 1.97(5) and 1.75(5) μB for **1** and **2**, respectively, which are consistent with the values obtained from the magnetic susceptibility measurements (see below) and the values reported previously.[27]

The temperature dependence of the magnetic susceptibility of the monomer **1** at higher temperatures could be described with the Curie–Weiss law, $\chi(T) = C/(T - \theta)$, in which the parameters C and θ are the Curie constant and the Weiss temperature, respectively (Figure 3). A leastsquares fit above 20 K yielded C = 0.43 emuK/mol and θ = –4.3 K. From the equation μeff2 = 8C, an effective magnetic moment μeff = 1.9 μB per Cu^{II} ion was obtained, which is in full agreement with the EPR results and the single-ion value.[27] A small negative value for θ suggests weak antiferromagnetic interactions between Cu^{II} ions. A relatively broad peak at Tmax = 2.9 K (Figure 3) indicates dimeric or some low-dimensional magnetic configuration. A look at the structure reveals that the Cu^{II} ions in neighboring monomers could be weakly coupled to build up pairs or chains (Figure S3). However, neither the Bleaney–Bowers model for an interaction between two local doublet states nor an alternating-spin chain model could

satisfactorily describe the low-temperature magnetic behavior of the monomer. Nevertheless, the interactions are much weaker than those for the dimer, as confirmed by a very low *T*max value. Compared with that of the monomer **1**, the temperaturedependent susceptibility of the dimer **2** exhibits a maximum at a significantly higher temperature *T*max = 7.3 K (Figure 3). It can be described by the Bleaney–Bowers model for an interaction between two local doublet states.[28] From a least-squares fit with the Bleaney–Bowers equation[28] over the whole temperature interval (Figure 3), we obtained J/kB = –6.14 K, g = 2.21, and ρ = 0.048, which are in good agreement with data for similar systems.[29,30]

Complex **3** shows paramagnetic-like behavior (Figure S14). The Curie–Weiss law was used to fit the zero-fieldcooled susceptibility curve above 20 K (Figure S14 inset). A value of 0.44 emuK/mol for *C* was obtained, from which an effective magnetic moment μeff = 1.8 μB was calculated, again in agreement with the literature value for a single ion. However, the derived value of +2.3 K for θ suggests weak ferromagnetic interactions between the Cu ions. Similarly to that of **1**, the susceptibility of **4** showed a maximum at low temperature (3.3 K), but the behavior could not be described by the Bleaney–Bowers model (Figure S15). Instead, the measured zero-field-cooled data was fitted by the Curie–Weiss model (Figure S15, inset). A Curie constant *C* = 0.42 emuK/mol and an effective magnetic moment μeff = 1.8 μB were obtained from the least-squares fit. The negative θ value of –3.1 K indicates weak antiferromagnetic interactions between the Cu ions.

Complex **5** shows paramagnetic-like behavior (Figure S16). By fitting the susceptibility curve with the Curie– Weiss law above 60 K (Figure S16, left inset), we obtained an effective magnetic moment μeff = 1.8 μB (*C* = 0.41 emu K/mol) and θ = +2.3 K. The latter is also reflected in the $\chi T(T)$ plot (Figure S16, right inset), which suggests ferromagnetic interactions

occur between the Cu ions at low temperatures, as further supported by a small hysteresis in the *M*(*H*) data measured at 2 K (Figure S17).

The room-temperature susceptibilities for all of the complexes are summarized in Table 2 and show a satisfactory agreement with the EPR data.

A considerable amount of work has been performed to correlate the structures of a large variety of chloridobridged copper(II) complexes and their magnetic properties. The magnetic properties of such systems depend on the nature of terminal ligands, the coordination geometry around the copper atoms, and the structural distortions from the ideal geometry. Among the possible structural types, we will focus here on pentacoordinate mono-μ-chlorido-bridged copper(II) chains (**3**) and di-μ-chlorido-bridged copper(II) dimers (**2** and **5**). For this μ-chlorido-bridged family of copper complexes, a rough dependence of the exchange coupling constant *J* on the *Φ*/*r* ratio is observed; *Φ* represents the angle at the bridging ligand atom (Cu–Cl–Cu), and *r* is the out-of-plane bond length (Cu–Cl).[31] For mono-μ- chlorido-bridged chains, if a value of *Φ* /*r* is in the range 40– 57°/Å, overall antiferromagnetic behavior can be expected, whereas ferromagnetic character is observed when this value is outside the range.[32] For di-μ-chlorido-bridged dimers, ferromagnetic exchange interactions occur if the value of *Φ*/*r* is in the range 32.6–34.8°/Å, otherwise the interaction is antiferromagnetic.[33]

To establish magnetostructural correlations for **1**–**5**, it is instructive to first take into account the relevant interactions in the crystal structures of the complexes. A common packing feature in the crystal structures of **1** and **4** (CSD refcode QOWWUV)[14,16] is that the monomer units are connected through alternating chlorine and nitrogen atoms from neighboring complex units to build up 1D chains parallel to the *a* axis (Figure S6). However, these contact distances are large and, thus, weak exchange interactions could be anticipated, as was confirmed by EPR

spectroscopy experiments. Both copper centers in the dimeric complex **2** have square-pyramidal geometries (τ_5 = 0.44), and the square pyramids share a base-to-apex edge with parallel basal planes; however, complex **5** (CSD refcode QOWXAC)[14,16] is an axial–equatorial dimer with the copper centers in a trigonal-bipyramidal environment (τ_5 = 0.71).[14] For dinuclear complex **2**, the value of Φ/r is 35.5°/ Å, which complies with the experimentally determined antiferromagnetic nature of the corresponding interactions. The value of Φ/r for **5** (37.7°/Å) implies that this complex should exhibit antiferromagnetic behavior, in contrast with the experimentally observed ferromagnetic behavior of the compound. However, this situation is similar to that found for the trigonal-bipyramidal copper(II) dihalo-bridged dimer [Cu2(Cl)2(dpt)2]Cl2 (dpt = dipropylenetriamine; Φ/r = 35.9°/ Å), which shows ferromagnetic coupling between the copper(II) ions as opposed to the established correlation.[29,34] As 1D polymeric chains form in the crystal structure of **3** (CSD refcode QOWWOP)[14,16] through weak coordinative bonds with the in-plane chlorido ligands from the neighboring complex units, the complex belongs to the mono-μ- chlorido chain type and has square-pyramidal geometry (τ_5 = 0.15).[14] Complex **3** has an Φ/r value of 37.9°/Å and shows ferromagnetic coupling, which fits the trend for mono-μ-chlorido chains.[32]

DFT Calculations

The DFT-optimized structures for **1**–**5** and the corresponding magnetic orbitals are shown in Figure 4. All of the optimized structures are in good agreement with the XRD data (Table S4). It is instructive to start with the orbitals of the monomer **1** (Figure 4). The singly occupied molecular orbital (SOMO) of the monomer has a very large contribution from the metal d orbitals; however, the largest spin density is located at the chlorido ligands. The overlap between the metal d_{x2-y2} orbital and the symmetry-adapted p orbitals of the chlorido ligands is frontal. As

the magnetic orbital of the copper atom is mainly delocalized in the equatorial plane, a very weak spin density can be expected at the axial position. Owing to the additional interactions with the chlorido ligands from the neighboring complex units, poor overlap at the bridging chlorido ligands is anticipated and, thus, weak antiferromagnetic coupling is expected, as observed experimentally. The same frontal overlap is observed for dinuclear complex **2** for one chlorido ligand in a basal coordination site, whereas the interaction with another chlorido ligand, which occupies an apex coordination site of the other Cu center, is of π* type between the Cu d_{x2-y2} and the apical Cl p orbitals. The consequence of such interactions is antiferromagnetic coupling with the exchange coupling constant J/kB (calcd.) = –9.05 K, which is in a good agreement with the experimentally obtained value of J/kB (exp.) = –6.14 K.

The SOMOs of the monomers **3** and **4** also have large contribution of d_{x2-y2}–metal orbitals and the p orbitals of the chlorine and nitrogen atoms, but the largest spin density is located at the chlorido ligands (Figure 4). The overlap between the Cu d_{x2-y2} orbital and the p orbitals of the chlorine and nitrogen atoms are of σ* type. The exchange coupling constant for the two monomer units of **3** mediated through one chlorine atom was calculated from the XRD structure, in which packing forces can induce small deviations from the minimum-energy geometries of individual molecules. In agreement with the experimental data, the DFT calculations predict ferromagnetic coupling (J/kB = 174.23 K) mediated through the chain comprised of the chlorine atoms between the two copper centers, which have a large Cu···Cu separation. To understand the experimentally observed antiferromagnetic coupling in **4**, packing interactions have to be taken into account again. Specifically, the copper atoms from neighboring monomeric units are connected through weak coordinative interactions with hydrazone nitrogen atoms to form dimers.[14] One copper magnetic orbital is parallel to that located on the other

copper center, which is separated from the former by 4.53 Å. The bridging hydrazone nitrogen atom is placed in the equatorial plane of one monomeric unit and occupies the apical position in the coordination sphere of the copper atom from the other monomeric unit. The possible magnetic coupling pathway involves interactions between the Cu orbitals and the nitrogen lone pair orbitals along the extended Cu–N–N···Cu linkage.

The DFT-optimized structure of **5** shows that the copper atoms are in a pentacoordinate trigonal-bipyramidal environment in which both d_{x2-y2} magnetic orbitals point to the p orbitals of the bridging Cl atom. Therefore, the magnetic exchange pathway involves a double Cu2–Cl bridge with an absolutely planar Cu2Cl2 core and a Cu···Cu distance of 3.55 Å. Accordingly, the calculated *J*/*kB* value of 162.20 K fits well with the magnetic susceptibility measurements, which showed ferromagnetic behavior for **5**.

DFT calculations generally provide a reliable estimate of the sign of the exchange interactions, but the derived magnitudes can deviate by several orders of magnitude depending on the calculation parameters.

The *g* values calculated for all complexes are in reasonable agreement with the experimental data (Table 2). In particular, the DFT method correctly predicts the *gxx* and *gyy* values but slightly underestimates *gzz*. These differences from the experimental *gzz* values are a rather general trend in the computed *g* matrices for all compounds and are not specific to one system, as observed previously for similar Cu^{II} compounds.[35] The calculated *gxx* and *gyy* values for the mononuclear complexes **1**, **3**, and **4** are only slightly different from those of typical square-planar Cu^{II} complexes (e.g., for the D_{4h} $CuCl_4^{2-}$ unit, *gxx*/*gyy* = 2.049).[36]

In vitro Cytotoxic Action of Copper Complexes 1–5

The antitumor potential of the copper complexes **1**–**5** was assessed against six tumor cell lines, namely, mouse fibrosarcoma (L929) and melanoma (B16), rat (C6) and human glioma (U251), and human glioblastoma (U87) and lung carcinoma (H460), through 3-(4,5-dimethythiazol-2- yl)-2,5-diphenyltetrazolium bromide (MTT) assays. The calculated IC50 values after 24 h exposure to each complex and the chemotherapeutic agent carmustine (BCNU), which is approved for the treatment of malignant glioma,[37] are presented in Table 3. Importantly, both **2** and **5** showed better antiglioma action than BCNU.

Dimeric Copper(II) Complexes Induce Oxidative Stress

The induction of oxidative stress by the hyperproduction of free radicals is involved in the cytotoxic action of previously reported polymeric copper(II) complexes.[38] As the complexes of interest in this study also contain copper centers, we wanted to explore if their cytotoxicity is also due to the copper-mediated induction of oxidative stress. Staining with the redox-sensitive fluorochrome dihydrorhodamine (DHR) revealed a dose-dependent increase in the production of reactive oxygen species (ROS) in C6 cells treated with both **2** and **5** (Figure 5), and **5** was somewhat more efficient than **2** (6.3- vs. 8.6-fold increase compared to untreated cells after 3 h treatment with **2** and **5**, respectively, in 30 μm concentration). These results confirm that oxidative stress contributes significantly to the cytotoxic action of dimeric copper(II) complexes on rat glioma cells.

Dimeric Copper(II) Complexes Cause Externalization of Phosphatidylserine, Caspase Activation, and DNA Fragmentation

We next investigated the type of cell death (apoptotic or necrotic) induced by the dimeric copper(II) complexes in rat glioma cells. Apoptosis is distinguished by phosphatidylserine exposure on the outer side of phospholipid bilayer of the cell membrane, caspase activation, and internucleosomal DNA fragmentation in the absence of plasma membrane damage, whereas plasma membrane breakdown characterizes necrotic cell death.[39] In our experiments, the flow cytometric analysis of C6 cells double-stained with annexin V/fluorescein isothiocyanate (FITC) and propidium iodide (PI) after 24 h treatment with **2** and **5** showed that both complexes caused externalization of phosphatidylserine on the outer side of phospholipid bilayer of plasma membrane. Complex **5** was again more efficient and caused an almost ninefold increase in the percentage of Ann+ cells in comparison with the control (from 2.4% in the control to 20.64% after treatment) compared with a fivefold increase (12.96% of Ann+ cells) after treatment with **2** (Figure 6, a). In addition, both complexes exerted more potent proapoptotic action than the prototypical antiglioma agent BCNU (Figure 6, a).

As both apoptosis pathways, extrinsic and intrinsic, can include activation of caspases, apoptosis-executing cysteine proteases,[40] we next investigated caspase activation in C6 glioma cells treated with the dimeric copper(II) complexes **2** and **5**. Our results (Figure 6, b) show an increase in pancaspase activity after 24 h treatment. Specifically, both **2** and **5** caused significant (1.8- and 1.9-fold, respectively) increases in the caspase-derived green fluorescence intensity after 30 μm treatment. Together with the externalization of phosphatidylserine, this result indicates the possible involvement of apoptosis in the cytotoxic action of dimeric copper(II) complexes.

Finally, we assessed the C6 cell-cycle distribution under the influence of the investigated complexes (30 μm). Even though 24 h treatment resulted in cell-cycle changes indicative of antiproliferative action (the accumulation of C6 cells in the G0/G1 phase), after 48 h, both **2** and **5** (30 μm) caused an increase in the percentage of rat glioma cells in the subG0 phase (from 1.08% in control to 6.92 and 12.10%, respectively), which is indicative of DNA fragmentation (Figure 6, c).

Conclusions

We have synthesized and characterized the copper(II) complexes [CuCl2(aphaOMe)] (**1**) and [Cu2Cl4(aphaOMe)2] (**2**). The obtained complexes are polymerized isomers, as revealed from XRD structure determination. Although the polymerized isomers are not readily interconvertible, the results indicate that the crystallization temperature partly plays a role in the final structure. The differences and similarities of the molecular and crystal structures of **1** and **2** to the existing structurally similar ones [CuCl2(fphaOEt)] (**3**), [CuCl2(aphaOEt)] (**4**), and [Cu2Cl4(qahaOEt)2] (**5**) are also reflected in their magnetic behavior, that is, complexes **1**, **2**, and **4** show antiferromagnetic coupling, whereas **3** and **5** exhibit ferromagnetic coupling between the central Cu^{II} atoms. In search of new potent cytotoxic complexes with multidentate hydrazone type ligands, we have evaluated the cytotoxic action of **1**–**5**. The monomeric complexes **1**, **3**, and **4** showed antitumor activity towards some of the cell lines investigated, whereas the dimeric complexes **2** and **5** were cytotoxic to all investigated tumor cell lines. The obtained results suggest that the antiglioma action of dimeric copper(II) complexes **2** and **5** involves oxidative-stress induction, followed by caspase activation and phosphatidylserine externalization. These

data could contribute to new therapy approaches and further research into this type of organic ligand and derived complexes as antitumor agents.

Experimental Section

General Remarks: 2-Acetylpyridine (2ap, 99+%), 2-formylpyridine (2fp, 98%), 2-quinolinecarbaldehyde (2qa, 97%), and $_{CuCl2}$·$2H_2O$ (p.a.) were obtained from Acros Organics, and ethyl hydrazinoacetate hydrochloride (haOEt·HCl, 97%) was obtained from Fluka. Solvents (methanol, ethanol, diethyl ether, and acetonitrile) were used without further purification. Elemental analyses (C, H, N) were performed by standard methods with an Elementar Vario ELIII analyzer. Molar conductivity measurements were performed at ambient temperature with a Crison Multimeter MM41. The IR spectra were recorded with a Thermo Scientific Nicolet 6700 FTIR spectrophotometer by the attenuated total reflection (ATR) technique in the region $\tilde{\nu}$ = 4000–400 cm^{-1}. Abbreviations used for IR spectra: vs, very strong; s, strong; m, medium; w, weak; br, broad; Py i.p., pyridine in plane; Py o.o.p., pyridine out of plane. The magnetic measurement at room temperature were performed by the Evans method by using an MSB-MK1 balance (Sherwood Scientific Ltd.) with Hg[Co(SCN)4] as a calibrant. Diamagnetic corrections were calculated from Pascal's constants. The UV/Vis (UV/ Vis) spectra were recorded with a GBC Scientific Cintra 6 UV/Vis spectrophotometer (200–1000 nm) with samples dissolved in DMSO and diluted with water such that the final DMSO content was 0.5% (v/v). Solid-state diffuse reflectance UV/Vis spectra were recorded with a Carl-Zeiss instrument with MgO as a standard. The conductometric electrode (Crison Platinum Cell 50 70 with an integrated Pt 1000

temperature sensor) was calibrated with Crison conductivity standards of conductivity 147 and 1413 μS/cm.

[CuCl2(aphaOMe)] (1) and [Cu2Cl4(aphaOMe)2] (2): A solution of haOEt·HCl (0.18 g, 1.16 mmol) and 2ap (0.14 g, 1.16 mmol) in methanol (20 mL) was heated with stirring until the temperature reached 40 °C, and then $CuCl_2·2H_2O$ (0.20 g, 1.16 mmol) was added. The reaction mixture was heated under reflux for 30 min and then cooled to ambient temperature. After 3 d, green crystals of **1** were obtained from the mother liquor; the crystals were collected by filtration and washed with cold ethanol and ether, yield 0.28 g (70.2%). $C_{10}H_{13}Cl_2CuN_3O_2$ (341.7): calcd. C 35.15, H 3.83, N 12.30; found C 34.92, H 3.74, N 12.39.
IR (ATR): $\tilde{\nu}$ = 3211 [m, ν(N–H)], 1749 [s, ν(C=O)], 1596 [m, ν(C=N)], 1222 [vs, ν(C–O)], 1021 [s, ν(N–N)], 647 (w, Py i.p.), 457 (w, Py o.o.p.) cm–1. Λ_M (1.1310–4 m, DMF): 12.93 Ω^{-1} cm^2mol^{-1}. μ(304 K) = 1.90 μB cm^{-1}. After the crystals of **1** were collected, the filtrate was left at ambient temperature. Brown crystals of **2** were obtained after 1 d. The crystals were recrystallized from methanol, collected by filtration, and washed with cold ethanol and diethyl ether. Crystals of **2** were also obtained from the mother liquor kept in a freezer, yield (crystals from the freezer): 0.20 g (50.5 %). $C_{20}H_{26}Cl_4Cu_2N_6O_4$ (683.4): calcd. C 35.15, H 3.83, N 12.30; found C 35.00, H 3.82, N 12.15. IR (ATR): $\tilde{\nu}$ = 3285 [w, ν(N–H)], 1728 [s, ν(C=O)], 1594 [vs, ν(C=N)], 1200 [vs, ν(C–O)], 1023 [s, ν(N–N)], 644 (w, Py i.p.), 456 (w, Py o.o.p.). Λ_M (1.1310–4 m, DMF): 11.33 Ω^{-1} cm^2mol^{-1}. μ(304 K) = 1.59 μB.

[CuCl2(fphaOEt)] (3), [CuCl2(aphaOEt)] (4), and [Cu2Cl4(qahaOEt)2] (5): Complexes **3**–**5** were prepared by template reactions of $CuCl_2·2H_2O$, 2fp/2ap/2qa, and haOEt·HCl, as described

previously.[14] The IR data, molar conductivity measurements, and elemental analysis results for **3**–**5** are in good agreement with the data previously reported.[14]

X-ray Crystallography: Powder samples of **1** and **2** were investigated by X-ray diffraction in a reflexive Bragg–Brentano θ–2θ geometry by using a conventional powder diffractometer (Seifert V-14) equipped with an automated high-temperature kit (Anton Paar HTK-10). The diffraction data was recorded by using Cu-$K\alpha$ radiation (λ = 1.54059 Å). All samples were recorded in continuous mode with an angular speed of 1°/min in the range 2θ = 5–30°. Suitable single crystals of **1** and **2** were mounted at the tip of a drawn-down glass capillary, and the X-ray data were collected at 293 K with an Xcalibur-Gemini S four-circle goniometer equipped with Sapphire CCD detector by using Mo-$K\alpha$ radiation (λ = 0.71073 Å). The data were reduced with the program CrysAlisPRO.[41] The data were corrected for Lorentz, polarization, and background effects.[41] The structures were solved by direct methods by using SIR-92[42] and refined by full-matrix least-squares procedures on $F2$ by using SHELXL-97[43] as implemented in the WinGX program suite.[44] Anisotropic displacement parameters were refined for all non-hydrogen atoms. The positions of the hydrogen atoms were derived from Fourier difference maps, except those of the methyl hydrogen atoms (in **2**), which were included at calculated positions riding on their attached atoms with fixed distances of 0.96 Å. However, in the final stages of the refinement, geometric constraints were applied along with isotropic displacement parameters. The final Fourier difference maps were featureless. The Cambridge Crystallographic Database[16] was used to evaluate and compare the derived structural models. CCDC-1052925 (for **1**) and -1052926 (for **2**), contain the supplementary crystallographic data for this paper.

These data can be obtained free of charge from The Cambridge Crystallographic Data Centre via www.ccdc.cam.ac.uk/data_request/cif.

Details of the data collection and the refinement are summarized in Table S1.

Magnetic Measurements: Continuous-wave EPR measurements were performed at room temperature with a home-built X-band (frequency ca. 9.4 GHz) spectrometer, equipped with a Varian E- 101 microwave bridge. For intensity calibration, a standard powder $CuSO_4 \cdot 5H_2O$ sample was used. Magnetic measurements were performed with a Quantum Design MPMS-XL 5 SQUID magnetometer. Temperature-dependent susceptibility $\chi(T) = M/H$ was measured between 2 and 300 K in a magnetic field H = 1000 Oe. The data were corrected for the contribution of the sample holder and the diamagnetic susceptibility of the inner-shell electrons. The susceptibility of the samples did not show any splitting between the zero-field-cooled (zfc) and field-cooled (fc) curves; thus, only the zfc data points are shown. Magnetization curves $M(H)$ were investigated at 2 K in magnetic fields up to 50 kOe.

Computational Details: DFT calculations were performed by using the ORCA software package.[45] Magnetic couplings in dinuclear complexes were calculated with the broken-symmetry approach developed by Noodleman et al.[46,47] In all calculations, the B3LYP functional coupled with the Ahlrichs (polarized) triple-ζ valence basis set (TZVPP) for Cu atoms and SVP basis set with one set of first polarization functions for N, C, H, O, and Cl atoms were used. The EPR g values were estimated with the B3LYP functional and IGLO-III basis set for all nonmetallic atoms and the TZVPP basis set for Cu atoms. We used the zeroth-order regular approximation (ZORA)[48] implemented in the ORCA code to calculate the EPR g values. The

exchange coupling constants, *J*, were estimated according to the Yamaguchi approach by using the equation $J = (E\text{HS} - E\text{BS})/[,S2.\text{HS} - ,S2.\text{BS}]$;[49] *E*HS is the energy of the highspin state, *E*BS is the energy of the broken-symmetry state, and <*S2*.HS and <*S2*.BS are the expectation values of the high-spin and broken-symmetry spin operators. If the metal centers are ferromagnetically coupled, *J* is positive because the highest spin state is lower in energy. On the contrary, antiferromagnetic coupling yields a negative value of *J*, and the lowest spin state is the ground state.

Cell Cultures and Reagents: The reagents used in the biological experiments were obtained from Sigma unless stated otherwise. The mouse fibrosarcoma (L929) and melanoma (B16) cell lines, rat (C6) and human glioma (U251), and human glioblastoma (U87) and lung carcinoma (H460) cell lines were obtained from the European Collection of Cell Cultures (ECACC). Cell cultures were maintained at 37 °C in a humidified atmosphere with 5 vol.-% CO2 in 4- (2-hydroxyethyl)-1-piperazineethanesulfonic acid (HEPES, 20 mm) buffered RPMI 1640 cell culture medium supplemented with 5% fetal calf serum, 2 mm l-glutamine, and 10 mm sodium pyruvate with the addition of penicillin/streptomycin mixture (all from PAA). The cells were prepared for the experiments by using the conventional trypsinization procedure with trypsin/ethylenediaminetetraacetic acid (trypsin/EDTA) and incubated in 96-well flat-bottom plates (13104 cells/well) for cell viability assessment or in six-well plates (303104 cells/well) for flow cytometric analysis. The cells were allowed to rest for 24 h and then treated with copper complexes **1**–**5** and BCNU dissolved in DMSO according to their solubility and afterwards diluted with nutrient medium to the desired final concentrations (up to 100 μm). The final concentration of DMSO was less than 0.5% (v/v). In each experiment, an additional control cell

culture contained the appropriate amount (maximum that was used) of solvent. As no differences were observed in comparison to the untreated cells, the results are presented only for the untreated cells as control.

Cytotoxic Assays: MTT assays for mitochondrial dehydrogenase activity were used to measure cell viability. The tests were performed as described previously,[50] and the results are presented with the control viability arbitrarily set to 100%. The IC50 values for the reduction of the tumor cell viability by the investigated compounds were determined by using GraphPad Prism.

Flow Cytometric Analysis of Cell Death Type, Cell Cycle, Caspase Activity, and Oxidative Stress: A minimum of 10000 cells were analyzed in each condition by flow cytometry analysis with a FACSCalibur flow cytometer (BD Biosciences) with the CellQuest Pro software for acquisition and analysis. The threshold settings were adjusted so that the cell debris was excluded from the data acquisition.

Oxidative Stress and ROS Production: The total intracellular production of reactive oxygen species (ROS) was determined by measuring the intensity of green fluorescence emitted by the nonselective redox-sensitive dye dihydrorhodamine 123 (DHR; Invitrogen), which was added to cell cultures (5 μm) at the beginning of the treatment. At the end of the incubation, the cells were detached by trypsinization and washed with phosphate-buffered saline (PBS), and the increase in green fluorescence (FL1) was analyzed as a measure of ROS production.

Apoptosis Assessment: The type of cell death (apoptotic or necrotic) was analyzed by double staining with annexin V/fluorescein isothiocyanate (FITC), which binds to early apoptotic cells

with exposed phosphatidylserine, and propidium iodide (PI), which labels the late apoptotic/necrotic cells with membrane damage (staining kit from BD Pharmingen). The activation of caspases was assessed by measuring the increase in the green fluorescence (FL1) of a cellpermeable FITC-conjugated pan-caspase inhibitor (ApoStat) according to the instructions provided by the manufacturer. The increase in green fluorescence (FL1) was considered as a measure of caspase activity.

Cell-Cycle Analysis: The cell-cycle analysis and determination of DNA fragmentation were performed by flow cytometric quantification of the nuclear DNA of ethanol-fixed cells stained with DNA binding dye (red fluorescent, FL2 channel) PI, as described previously.[50]

Statistical Analysis: The analysis of the statistical significance of the differences was performed by Student *t* tests for small independent samples. A value of p,0.05 was considered significant.

Supporting Information (see footnote on the first page of this article): Diffractograms for **1** (Figure S1) and **2** (Figure S2) obtained on heating; crystal data and structure refinement details for **1** and **2** (Table S1); capped-stick representations of the crystal packing of **1** (Figure S3) and **2** (Figure S4); C–H···O interaction parameters for **2** (Table S2); least-squares fits of the aromatic frames of **1** and **4** (Figure S5); crystal packing of **1** and **4** (Figure S6); least-squares fits of the aromatic frames of **1** and **3** (Figure S7); least-squares fits of the Cu–(μ-Cl)$_2$–Cu skeletons of **2** and **5** (Figure S8); electronic absorption spectra of **1**–**5** (Figure S9); electronic spectroscopic data for **1**–**5** (Table S3); aqueous solution behavior of **1**–**5** studied by UV/Vis spectroscopy (Figure S10); plots of molar conductivity versus time for **1**–**5** (Figure S11); solid-state and solution

UV/Vis spectra of **1** and **2** (Figure S12); EPR spectra of **1**–**5** (Figure S13); temperature dependence of zfc and fc susceptibility for **3**–**5** (Figures S14–S16); magnetization curve for **5** measured at 2 K (Figure S17); DFT optimization results for **1**–**5** (Table S4).

Acknowledgments

This work was supported by the Ministry of Education, Science, and Technological Development of the Republic of Serbia (grant numbers OI 172055 and III 41025).

[1] C. Santini, M. Pellei, V. Gandin, M. Porchia, F. Tisato, C. Marzano, *Chem. Rev.* **2014**, *114*, 815–862.

[2] J. Tan, B. Wang, L. Zhu, *J. Biol. Inorg. Chem.* **2009**, *14*, 727–739.

[3] A. Chakraborty, P. Kumar, K. Ghosh, P. Roy, *Eur. J. Pharmacol.* **2010**, *647*, 1–12.

[4] X. Qiao, Z.-Y. Ma, C.-Z. Xie, F. Xue, Y.-W. Zhang, J.-Y. Xu, Z.-Y. Qiang, J.-S. Lou, G.-J. Chen, S.-P. Yan, *J. Inorg. Biochem.* **2011**, *105*, 728–737.

[5] M. R. Maurya, R. Mannar, S. Agarwal, M. Abid, A. Azam, C. Bader, M. Ebel, D. Rehder, *Dalton Trans.* **2006**, *7*, 937–947.

[6] M. Carcelli, P. Mazza, C. Pelizzi, G. Pelizzi, F. Zani, *J. Inorg. Biochem.* **1995**, *57*, 43–49.

[7] C. Amort, M. Malaun, A. Krajete, H. Kopacka, K. Wurst, M. Christ, D. Lilge, M. O. Kristen, B. Bildstein, *Appl. Organomet. Chem.* **2002**, *16*, 506–516.

[8] P. Liu, W. Zhang, R. He, *Appl. Organomet. Chem.* **2009**, *23*, 135–139.

[9] M. R. Filipović, A. C. W. Koh, S. Arbault, V. Niketić, A. Debus, U. Schleicher, C. Bogdan, M. Guille, F. Lemaitre, C. Amatore, I. Ivanovic´-Burmazovic´, *Angew. Chem. Int. Ed.* **2010**, *49*, 4228–4232.

[10] K. V. Shuvaev, L. N. Dawe, L. K. Thompson, *Dalton Trans.* **2010**, *39*, 4768–4776.

[11] N. R. Filipović, A. Bacchi, G. Pelizzi, R. Marković, D. Mitić, K. K. Aneelković, *J. Coord. Chem.* **2005**, *58*, 1541–1550.

[12] N. R. Filipović, T. R. Todorović, D. M. Sladić, I. T. Novaković, D. A. Jeremić, K. K. Aneelković, *Mater. Sci. Forum* **2007**, *555*, 423–428.

[13] N. Filipović, T. Todorović, R. Marković, A. Marinković, S. Tufengdžić, D. Gođevac, K. Aneelković, *Trans. Met. Chem.* **2010**, *35*, 765–772.

[14] N. Filipović, H. Borrmann, T. Todorović, M. Borna, V. Spasojević, D. Sladić, I. Novaković, K. Anđelković, *Inorg. Chim. Acta* **2009**, *362*, 1996–2000.

[15] N. Filipović, T. Todorović, D. Radanović, V. Divjaković, R. Marković, I. Pajić, K. Aneelković, *Polyhedron* **2012**, *31*, 19–28.

[16] F. H. Allen, *Acta Crystallogr., Sect. B* **2002**, *58*, 380–388.

[17] a) The parameter $\tau 4$ is an index for four-coordinate complexes, $\tau 4 = [360° - (\alpha + \beta)]/141°$; α and β are the two largest bond angles; b) L. Yang, D. R. Powell, R. P. Houser, *Dalton Trans.* **2007**, 955–964.

[18] a) The parameter $\tau 5$ [$\tau 5 = (\beta - \alpha)/60°$; $(\beta - \alpha)$ is the difference of in-plane *trans* bond angles] is an index of the degree of trigonality within the structural continuum between trigonal-bipyramidal and square-pyramidal geometry; b) A. W. Addison, T. N. Rao, J. Reedijk, G. C. Verschoor, *J. Chem. Soc., Dalton Trans.* **1984**, 1349–1356.

[19] M. B. Ferrari, G. G. Fava, P. Tarasconi, C. Pelizzi, *J. Chem. Soc., Dalton Trans.* **1989**, 361–366.

[20] P. G. Beckingsale, A. T. Morcom, C. E. F. Rickard, T. N. Waters, *J. Chem. Soc., Dalton Trans.* **1977**, 2135–2138.

[21] a) The displacement was measured by the angle formed between the vector through the centroids of the respective rings and a vector normal to the ring planes, see: b) C. Janiak, *J. Chem. Soc., Dalton Trans.* **2000**, 3885–3896.

[22] S. F. Haddad, J. Piekardt, *Trans. Met. Chem.* **1993**, *18*, 377– 384.

[23] J. M. Rowland, M. M. Olmstead, P. K. Mascharak, *Inorg. Chem.* **2000**, *39*, 5326–5332.

[24] S. Naiya, C. Biswas, M. G. B. Drew, C. J. Gómez-García, J. M. Clemente-Juan, A. Ghosh, *Inorg. Chem.* **2010**, *49*, 6616–6627.

[25] P. F. Raphael, E. Manoj, M. R. Prathapachandra Kurup, *Polyhedron* **2007**, *26*, 818–828.

[26] A. B. P. Lever, *Inorganic Electronic Spectroscopy*, 2nd ed., Elsevier Science, New York, **1984**, p. 568.

[27] N. W. Ashcroft, N. D. Mermin, *Solid State Physics*, 1st ed., Saunders College, Philadelphia, **1976**, p. 658.

[28] B. Bleaney, K. D. Bowers, *Proc. R. Soc. London Ser. A* **1952**, *214*, 451–465.

[29] M. C. Aguirre, J. Borras, A. Castiñeiras, J. M. García-Monteagudo, I. García-Santos, J. Niclós, D. X. West, *Eur. J. Inorg. Chem.* **2006**, 1231–1244.

[30] A. Elmali, *Turk. J. Phys.* **2000**, *24*, 667–672.

[31] W. E. Hatfield, *Comments Inorg. Chem.* **1981**, *1*, 105–121.

[32] W. A. Alves, I. O. Matos, P. M. Takahashi, E. L. Bastos, H. Martinho, J. G. Ferreira, C. C. Silva, R. H. de Almeida Santos, A. Paduan-Filho, A. M. Da Costa Ferreira, *Eur. J. Inorg. Chem.* **2009**, 2219–2228.

[33] W. E. Hatfield, in: *Magneto-Structural Correlations in Exchange Coupled Systems* (Eds.: R. D. Willett, D. Gatteschi, O. Kahn), NATO ASI Series C, Reidel, Dordrecht, The Netherlands, **1985**, vol. 140, p. 555.

[34] R. Rodríguez, A. Llobet, M. Corbello, A. E. Martell, J. Reibenspies, *Inorg. Chem.* **1999**, *38*, 2328–2334.

[35] K. Wojciechowski, A. Bitner, G. Bernardinelli, M. Brynda, *Dalton Trans.* **2009**, *7*, 1114–1122.

[36] C. Chow, K. Chang, R. D. Willett, *J. Chem. Phys.* **1973**, *59*, 2629–2640.

[37] V. A. Venur, D. M. Peereboom, M. S. Ahluwalia, *Cancer Treat. Res.* **2015**, *163*, 103–115.

[38] V. M. Leovac, G. A. Bogdanović, L. S. Jovanović, L. Joksović, V. Marković, M. D. Joksović, S. M. Denčić, A. Isaković, I. Marković, F. W. Heinemann, S. Trifunović, I. Đalović, *J. Inorg. Biochem.* **2011**, *105*, 1413–1421.

[39] A. L. Edinger, C. B. Thompson, *Curr. Opin. Cell Biol.* **2004**, *16*, 663–669.

[40] R. C. Taylor, S. P. Cullen, S. J. Martin, *Nat. Rev. Mol. Cell Biol.* **2008**, *9*, 231–241.

[41] Agilent, *CrysAlis PRO*, Agilent Technologies, Yarnton, **2010**.

[42] A. Altomare, M. C. Burla, G. Camalli, G. Cascarano, C. Giacovazzo, A. Gualiardi, G. Polidori, *J. Appl. Crystallogr.* **1994**, *27*, 435–436.

[43] a) G. M. Sheldrick, *SHELXS-97 and SHELXL-97, Programs for Solution and Refinement of Crystal Structures from Diffraction Data*, University of Göttingen, Germany, **1997**; b) G. M. Sheldrick, *Acta Crystallogr., Sect. A* **2008**, *64*, 112–122.

[44] L. J. Farrugia, *J. Appl. Crystallogr.* **1999**, *32*, 837–838.

[45] F. Neese, *Orca, an ab initio, DFT and Semiempirical Electronic Structure Package*, version 2.8, revision 15, Max Planck Institute for Bioinorganic Chemistry, Mülheim/Ruhr, Germany, **2009**.

[46] L. Noodleman, C. Y. Peng, D. A. Case, J. M. Mouesca, *Coord. Chem. Rev.* **1995**, *144*, 199–244.

[47] a) L. Noodleman, D. A. Case, A. Aizman, *J. Am. Chem. Soc.* **1988**, *110*, 1001–1005; b) L. Noodleman, J. G. Norman, J. H. Osborne, A. Aizman, D. A. Case, *J. Am. Chem. Soc.* **1985**, *107*, 3418–3426; c) L. Noodleman, *J. Chem. Phys.* **1981**, *74*, 5737– 5743.

[48] E. Vanlenthe, E. J. Baerends, J. G. Snijders, *J. Chem. Phys.* **1993**, *99*, 4597–4610.

[49] a) T. Soda, Y. Kitagawa, T. Onishi, Y. Takano, Y. Shigeta, H. Nagao, Y. Yoshika, K. Yamaguchi, *Chem. Phys. Lett.* **2000**, *319*, 223–230; b) K. Yamaguchi, Y. Takahara, T. Fueno, in: *Applied Quantum Chemistry* (Eds.: V. H. Smith Jr., H. F. Schaefer III, K. Morokuma), Reidel, Dordrecht, The Netherlands, **1986**, p. 155.

[50] N. Raicević, A. Mladenović, M. Perović, L. Harhaji, D. Miljković, V. Trajković, *Neuropharmacology* **2005**, *48*, 720–731.

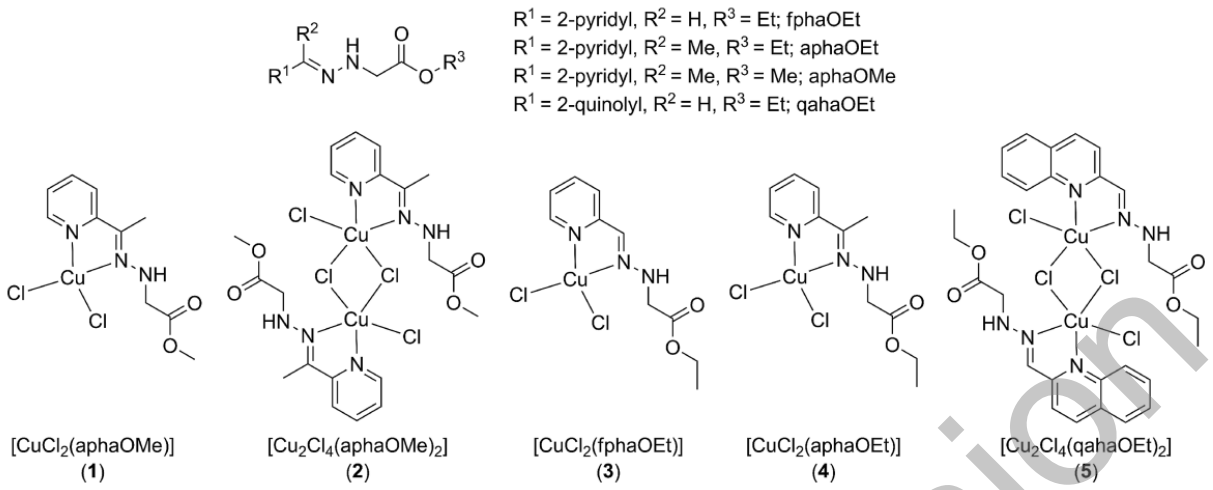

Scheme 1. N-Heteroaromatic hydrazone ligands derived from ethyl hydrazinoacetate and the corresponding copper complexes **1**–**5**.

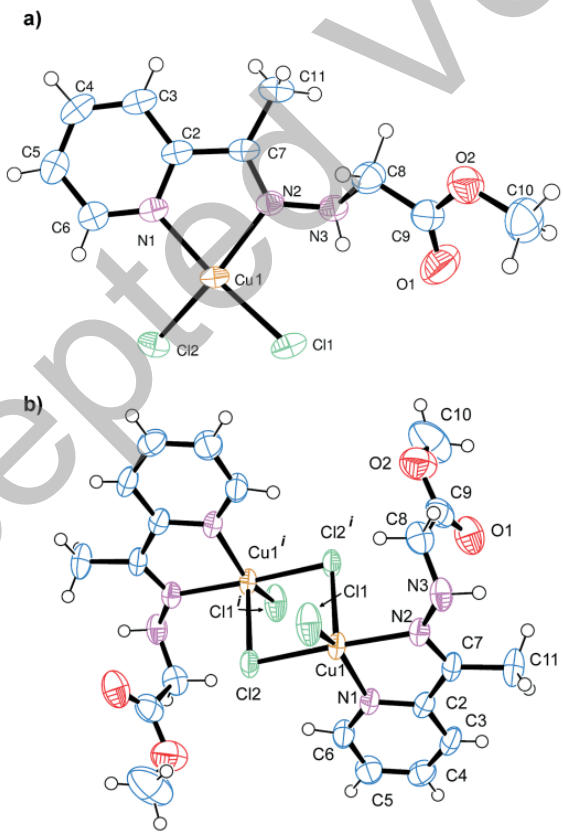

Figure 1. Molecular structures of (a) **1** and (b) **2**. The ellipsoids are drawn on the 50% probability level, and hydrogen atoms are depicted at an arbitrary size.

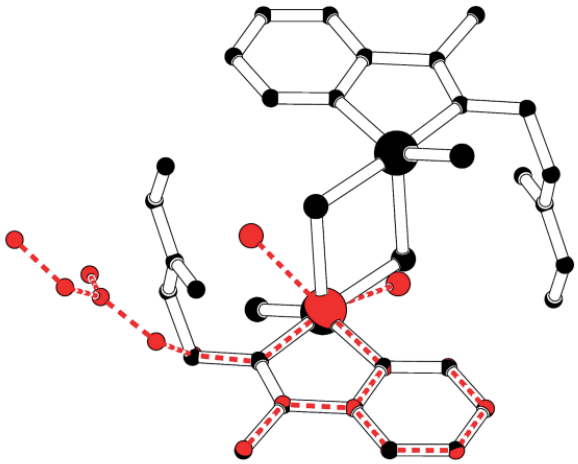

Figure 2. The result of least-squares fits of the aromatic frames of **1** and **2**. Hydrogen atoms have been omitted for clarity. The main directions of the side chains are separated by 64.5°.

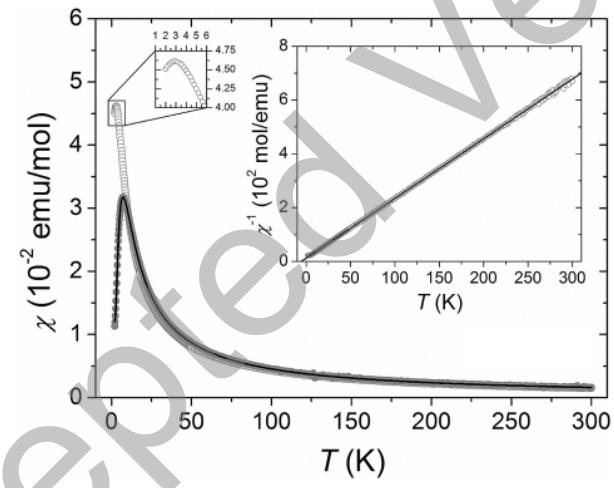

Figure 3. Plots of magnetic susceptibility versus temperature for **1** (open symbols) and **2** (full symbols). Inset: inverse magnetic susceptibility for **2** as a function of temperature. The solid lines are reproduced from the detailed fitting procedure described in the text.

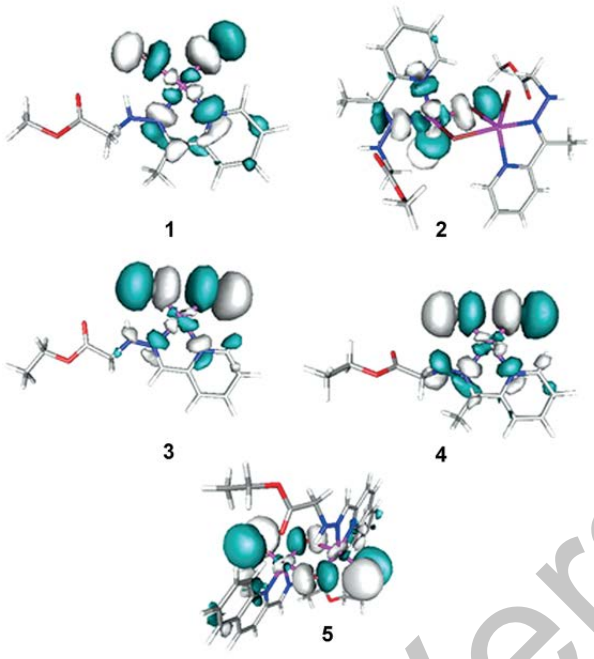

Figure 4. Magnetic orbitals of **1**–**5**.

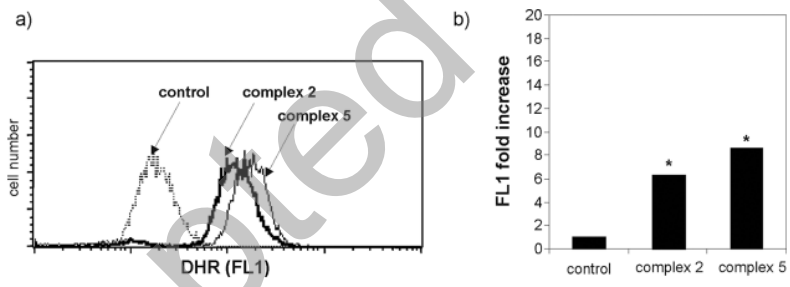

Figure 5. Dimeric copper(II) complexes induce ROS production in C6 rat glioma cells. (a) Representative histogram for the increase in DHR-derived mean FL1 fluorescence intensity after 3 h treatment with 30 μm of **2** and **5**. (b) Representative bar chart showing the 6.3- and 8.6-fold increases in the DHR-fluorescence intensity after treatment (3 h; 30 μm) with **2** and **5**, respectively (* *p*,0.05 in comparison with control).

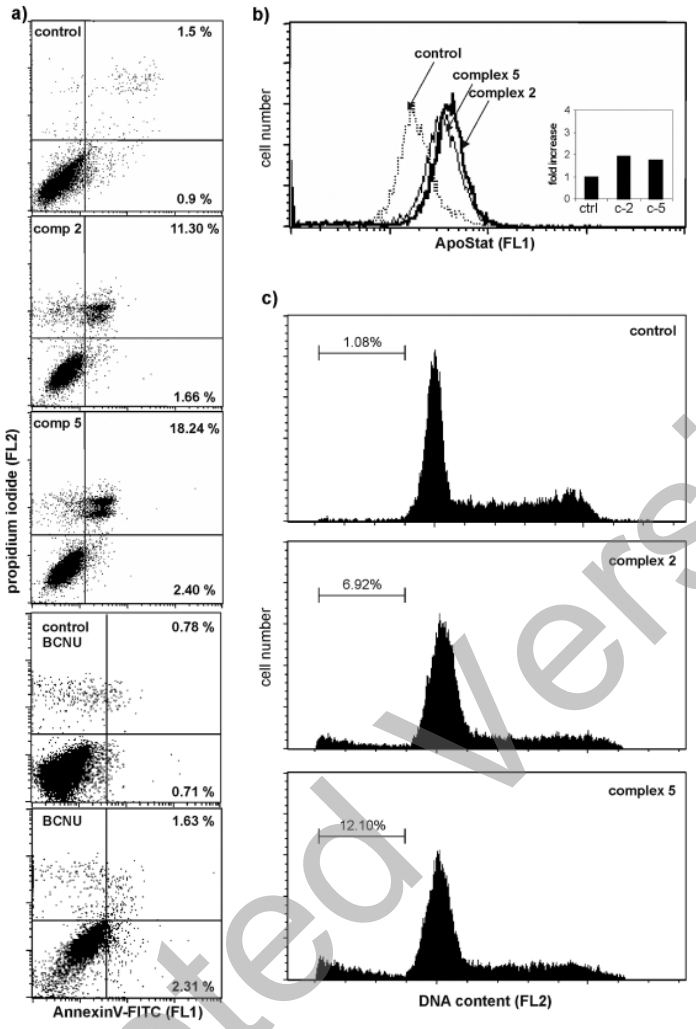

Figure 6. Dimeric cooper(II) complexes cause externalization of phosphatidylserine, caspase activation, and cell-cycle disturbance in C6 rat glioma cells. (a) Representative dot-plots of double Annexin V–FITC and PI stained control cells and cells treated (24 h; 30 μm) with **2**, **5**, or BCNU (24 h, 60 μm). (b) Representative histogram showing the increase in caspase activation, evidenced by the increase in the FL1 mean fluorescence intensity in C6 cells treated with **2** and **5** (30 μm; 24 h). (c) Representative histograms of cellcycle distribution of C6 cells following treatment with **2** and **5** (48 h, 30 μm) showing the increase in the percentage of cells in the sub-G0 phase of the cell cycle.

Table 1. Comparison of selected bond lengths [Å] and angles [°].

	1	**2**
Cu(1)–N(1)	1.999(2)	2.019(3)
Cu(1)–N(2)	2.032(2)	2.043(3)
Cu(1)–Cl(2)	2.2441(10)	2.2812(9)
Cu(1)–Cl(1)	2.2471(9)	2.2400(9)
Cu(1)–Cl(2)^{i}[a]	–	2.6636(9)
C(2)–C(7)	1.463(4)	1.470(5)
C(7)–N(2)	1.291(4)	1.292(4)
N(2)–N(3)	1.389(4)	1.379(4)
N(3)–C(8)	1.450(4)	1.434(5)
N(1)–Cu(1)–N(2)	79.34(10)	79.28(11)
N(1)–Cu(1)–Cl(1)	165.06(8)	146.08(8)
N(2)–Cu(1)–Cl(1)	93.83(7)	95.03(8)
N(1)–Cu(1)–Cl(2)	95.04(8)	94.35(8)
N(1)–Cu(1)–Cl(2)^{i}	–	99.82(7)
N(2)–Cu(1)–Cl(2)	161.23(7)	172.43(8)
Cl(1)–Cu(1)–Cl(2)^{i}	–	113.82(4)
C(7)–N(2)–N(3)	120.9(3)	119.8(3)
C(7)–N(2)–Cu(1)	116.7(2)	115.8(2)
N(3)–N(2)–Cu(1)	122.40(18)	123.3(2)
C(2)–C(7)–N(2)	114.3(3)	114.9(3)
N(1)–C(2)–C(7)	115.2(2)	115.3(3)
Cl(2)–Cu(1)–Cl(2)^{i}	–	85.57(3)
Cu(1)–Cl(2)–Cu(1)^{i}	–	94.43(3)

[a] Symmetry code for **2**: (*i*) $-x + 2, -y + 1, -z + 1$

Table 2. Experimental (EPR) and DFT-calculated (in parentheses) *g* tensors for **1**–**5** along with the experimental full width at halfmaximum (ΔHFWHM) and intensity (χEPR) values for the EPR signals. The EPR results were obtained at room temperature. For comparison, the room-temperature magnetic susceptibility χSQUID values are also listed.

	1	**2**	**3**	**4**	**5**
g_{xx}	2.050 (2.037)	2.045 (2.040)	2.120 (2.068)	2.046 (2.046)	2.046 (2.032)
g_{yy}	2.050 (2.037)	2.114 (2.090)	2.124 (2.068)	2.053 (2.048)	2.114 (2.103)
g_{zz}	2.232 (2.116)	2.189 (2.120)	2.175 (2.152)	2.230 (2.149)	2.334 (2.220)
g_{iso}[a]	2.063	2.083	2.096	2.081	2.118
ΔH_{FWHM} [G]	50	110	250	35	305
$\chi_{EPR} \times 10^{-3}$[b]	1.3(2)	1.6(2)	1.0(2)	1.5(2)	1.8(2)
$\chi_{SQUID} \times 10^{-3}$[b]	1.5	1.6	1.4	1.4	1.4

[a] Calculated $g_{iso} = (g_{xx} + g_{yy} + g_{zz})/3$. [b] In emu/mol (Cu).

Table 3. In vitro cytotoxicity (IC50 in μm)[a] of copper(II) complexes **1**–**5** and BCNU determined by MTT assay after 24 h incubation.

	1	**2**	**3**	**4**	**5**	BCNU
L929	83.5 ± 1.6	81.1 ± 0.8	43.2 ± 1.4	88.8 ± 0.9	69.4 ± 1.1	n.a.[b]
C6	63.3 ± 1.2	43.6 ± 0.9	17.7 ± 2.1	16.9 ± 1.9	27.9 ± 2.3	56.7 ± 3.3
U251	>100	22.6 ± 0.5	>100	>100	65.6 ± 1.2	221.4 ± 9.3
B16	>100	58.8 ± 0.9	>100	>100	53.3 ± 1.5	n.a.
H460	88.8 ± 0.5	95.3 ± 0.9	>100	84.3 ± 0.6	43.1 ± 1.1	n.a.
U87	77.6 ± 1.8	36.6 ± 2.1	>100	85.5 ± 0.7	58.9 ± 2.2	87.6 ± 9.8

[a] The values represent the mean 6standard deviation (SD) from two independent experiments.

[b] n.a.: not assessed.